**Research article**

# Performance analysis of WSe₂-based bifacial solar cells with different electron transport and hole transport materials by SCAPS-1D

M. Atowar Rahman [*]

*Department of Electrical and Electronic Engineering, University of Rajshahi, Rajshahi-6205, Bangladesh*

A B S T R A C T

In recent years, solar cells made of tungsten diselenide (WSe₂) have received comprehensive consideration because of their good photoelectric properties. The planar WSe₂-based heterojunction solar cell with a preliminary device structure of Au/WSe₂/electron transport layer (ETL)/FTO/Al was designed and investigated numerically by SCAPS-1D. CdS ETL is widely used in thin film solar cells (TFSCs). Due to environmental issues and the low band gap (2.42 eV) of CdS ETL, an alternative to CdS ETL was being explored for WSe₂ solar cells. In this work, the photovoltaic (PV) performance of the WSe₂-based TFSCs with different ETLs were simulated, analyzed and compared, in an attempt to track down a suitable substitute for the CdS ETL. In addition to CdS ETL, ZnO, TiO₂ and SnO₂ ETLs were independently used to simulate the PV performance of WSe₂-based TCSCs. In the wake of analyzing the J-V curves of different cell configurations, SnO₂ ETL yielded the best results with PCE of 27.14 % for the single-junction WSe₂/SnO₂ TFSC. Then, our simulation predicted that the PV performance of the WSe₂ device can be improved significantly by using N doped Cu₂O as a hole transport layer (HTL). The optimized WSe₂ device with SnO₂ ETL and Cu₂O:N HTL showed an improved PCE of 33.84 % with very good performance stability at higher temperature. Furthermore, this article proposes to use the Au/Cu₂O:N/WSe₂/SnO₂/FTO/Al heterojunction solar cell in bifacial mode and PV performance of the proposed bifacial device have been also studied using SCAPS-1D. Bifacial WSe₂ device leads to enhanced PV performance with bifaciality factor for PCE is 83.64 %. Bifacial gain of the proposed device under simultaneous irradiation of 1 sun from the front and 20 % of 1 sun from back side is found to be 13.95 %. Our simulation predicts that the proposed WSe₂ bifacial solar cell is capable of converting solar energy into electricity with an efficiency of about 38.38 %.

## 1. Introduction

The fast growth of world energy demand and the increasing global pollution as well as the decreasing conventional energy resources clearly demonstrate the need to provide affordable and sustainable clean energy supplies. There are not many resources that can meet the power demand of the tera-watts (TW) scale by 2050. Solar energy is considered as the main compelling alternatives that can meet the demand of 15 TW with a huge amount of solar energy to spare [1], and solve the world energy crisis and reduce the environmental problems. A potentially effective way to harness solar energy is to use photovoltaic (PV) devices called solar cells (SCs) to convert it directly into electricity. The PV technology is relatively simple, with no moving parts or necessary subsystems, which makes it relatively easy to expand to the TW level. The first SC made of Si was reported in the 1950s [2], and recently, its efficiency reached a record 26.1% in 2020 [3]. In the 1970s, many inorganic solar energy

absorbing materials were considered to be able to produce high-efficiency SCs. However, in practice, few of them such as CdTe and CIGS SCs have their power conversion efficiency (PCE) exceeding 20% [4]. However, the environmental impact of *Cd* and the inadequacy of *Te, In,* and *Ga* are major issues for the widespread commercialization of these devices. Since then, the number of suitable absorbers has been increasing [5] and in 1988, CZTS/CZTSe stood out from the ongoing investigation of absorber materials for being composed of low-cost, earth-abundant, and nontoxic elements. At present, the PCE of CZTS/CZTSSe devices has advanced to 13.0 % in 2021 [3], which is far behind the CdTe and CIGS-based devices. Very recent theoretical studies predict that 31 % PCE of CZTS/CTSe-based SCs can be achieved by engineering the conduction band edges between the buffer and the absorber layer to reduce non-radiative recombination at the interfaces and utilizing the back surface field layer between the back-electrode and absorber layer [6, 7]. In recent years, the emergence of hybrid perovskite SCs is noticeable

because of their suitable optoelectrical properties, low fabrication costs, and its efficiency cross-over the commercialization demarcation line and ramped up to 25.5 % level in just a few years [3]. However, there are many challenges such as hysteresis, long-term stability and sensitivity to moisture, and toxicity associated with perovskite SCs which degrade its performance [8, 9, 10].

Tungsten diselenide (WSe₂) has a three-layers microstructure of selenium (Se)-tungsten (W)–Se, in which the interlayer is bonded by a weak van der Waals force, which allows to effectively tune their electrical and optical properties by suitable doping. It was first identified as a possible PV absorber material in the 1970s [11, 12, 13]. It has the optimal band gap of 1.35–1.58 eV [14] for single and double junction SCs, very high optical absorption in the near infra-red and visible region [12, 15, 16], high carrier mobility [12], tunable carrier concentration, and low thermal conductivity [17]. More importantly, it has eminently high chemical phase purity with only one stable phase at room temperature [18] and is very stable in acidic solutions [19]. Recently, TMDCs have attracted enormous consideration owing to their low-cost and superior electrochemical [20, 21], optical [22], mechanical [23], and thermal properties [17]. Hence, it is of a great scientific interest as an active layer for thin film SCs. TMDCs have also been investigated as electrodes for photoelectrochemical SCs [24]. A special feature of layered-type materials is the low surface defect density of the van der Waals planes [25], which is a potential advantage for the use of such materials to prepare heterojunctions for optoelectronic and PV applications [26].

Different methods such as soft selenization [15, 27], high temperature selenization [28], physical vapor transport [29], chemical bath deposition [30], electrodeposition [31], pulsed laser deposition [32], Se–oxygen ion exchange [33], and atmospheric pressure chemical vapor deposition [34], have been used successfully to synthesize high quality WSe₂ thin films. Recently, Hongchao Li et al. have demonstrated an environmentally friendly method to prepare WSe₂ films with different orientations on the non-conductive quartz glass [35, 36]. Although WSe₂ thin films have many applications, such as p-n diodes [37], field-effect transistors [38], and logic devices [39, 40], there are only a few reports that have proven its application in PV SCs so far [41, 42, 43].

In view of all of these aforementioned favorable properties of WSe₂ thin films as absorber materials of TFSCs, we adopt crystalline-WSe₂-based heterojunction PV devices with different junction partners using SCAPS-1D SC simulator to simulate its PV performance. In this work, several ETL materials namely CdS, ZnO, TiO₂, and SnO₂ were studied and four WSe₂-based TFSCs with the preliminary structure of SLG/Au/WSe₂/ETL/FTO/Al were implemented in the SCAPS-1D environment to analyze their PV performances. The J-V characteristics of the SCs have been calculated for different ETLs to compare their PV performance and select suitable ETL for WSe₂-based SCs.

The PV performance of WSe₂ SCs is hindered by many reasons. For instance, the PV performance of the SCs is limited by the high recombination of minority carriers at the back contact. The passivation of the back contact can improve the PV performance of the device. This can be achieved by the back surface field (BSF) concept of introducing a highly doped p⁺-type semiconductor between the back contact and the WSe₂ absorber layer. Therefore, the electric field at the $p^+$-$p$ junction acts as a potential barrier for the photogenerated electrons and repels back toward the $p$-$n$ junction, which leads to a reduction in recombination of minority carriers at the back contact. Nitrogen-doped Cu₂O (Cu₂O:N) has high acceptor density, earth-abundant elements, low-cost, and low-temperature synthesis process, making it a suitable candidate as BSF/HTL layer for WSe₂ based SCs. In this simulation, with the aim to reduce minority carrier recombination and enhance photogenerated holes collection at the back contact, the effect of introducing Cu₂O:N HTL into the WSe₂ SCs with the configuration of SLG/Au/Cu₂O:N/WSe₂/ETL/FTO/Al has been studied. The impact of the thickness and carrier concentration of different layers of the proposed WSe₂-based device with Cu₂O:N HTL and without Cu₂O:N HTL are also studied. At last, we examine the viability of the proposed WSe₂-based

device with Cu₂O:N HTL to use as a bifacial SC with further improved PV performance.

## 2. Numerical modeling and simulation parameters

The simulation can reproduce the outcomes of physical device which can be investigated by varying input conditions. The study of the proposed physical model or device by numerical simulation is a basic method to understand the operation of the device, and predicts how the device parameters immediately affect the physical operation and performance of the device without spending a lot of money and wait a long time. Planar WSe₂-based heterojunction TFSCs with a preliminary structure of SLG/back contact (Au)/WSe₂/ETL/FTO/front-contact (Al) was adopted in SCAPS-1D environment and analyzed the PV performance of devices. SCAPS-1D is based upon the solution of three governing transport equations in semiconductor; Poisson's equation, continuity equations for free electrons, and holes [44]. SCAPS simulator firstly solves these three coupled differential equations at one-dimensional steady-state conditions, and then calculates quasi-Fermi levels and electrostatic potential of carriers (free electrons and holes) at all points in the SC, and finally calculates the carrier concentration, electric field and other device performance parameters. The relative accuracy of results acquired by simulation depends on precise selection of parameters of materials used in each layer of the device. In this simulation, the material parameters of each layer of the device are selected precisely from authentic literature. In some circumstances, the input parameters are taken from reasonable assumptions to reflect the possible results under actual experimental conditions. The parameters for each layer of the device and the baseline value of each parameter which is used to carry out the simulation are tabulated in Table 1. In the bulk region of each semiconductor layer of the device, a single-level defect (donor/acceptor) with Gaussian energetic distribution is introduced and bulk defect density of each layer of the device is listed in Table 1. The hole and electron capture cross-section for defects in the WSe₂ layer are computed as: $\sigma = 1/(n_t v \tau)$ cm²; where $n_t$ is the defect density in the WSe₂ layer ($10^{14}$ cm⁻³), $v$ is the thermal velocity of electron ($1.7 \times 10^7$ cm/s) and hole ($1.4 \times 10^7$ cm/s) [56], and $\tau$ is carrier lifetime in the WSe₂ absorber layer.

Early reports shows that the value of the carrier lifetime in c-WSe₂ thin films is in the range of 6–30 ns [60, 61]. As a first approximation, we used an average value of approximately 16 ns for the carrier lifetime in the WSe₂ thin films. Therefore, the calculated values of electron and hole capture cross-section for defects in the WSe₂ layer are $3.67 \times 10^{-14}$ cm² and $4.46 \times 10^{-14}$ cm² respectively. Losses due to recombination at each interface are accounted for by introducing reasonable neutral interface defects, shown in Table 1. The characteristic features of the front and back-contact materials are work function, reflectivity, and surface recombination velocity, etc. The reflectivity at the front and back contact are considered to be 10 % and 90 % respectively, while other properties of the front-contact, back-contact, and working temperature are provided in Table 2. In this simulation, the experimental optical absorption coefficient of the WSe₂, Cu₂O:N, and different ETLs are taken from the literature [50, 62, 63, 64, 65, 66]. The device is irradiated with a standard AM 1.5G solar spectrum at the power of 100 mW/cm². In the simulation process, as the shunt and series resistances allow to consider the recombination or leakages losses in solar cells, the reasonable values of 1000 Ω.cm² and 2.5 Ω.cm² for the shunt and series resistances, respectively, are considered to realize the real device. In this work, 300 K is assumed to the normal operating temperature of the device.

## 3. Results and discussion

### 3.1. Effect of different ETLs on the performance of WSe₂ solar cells

In order to generate an adequate field at the absorber/ETL junction, the role of the ETL is very important. More importantly, the energy band edges of ETL affect the band offset at the interface, thereby affecting carrier transport. In addition, the ETL can prevent shunting between the

**Table 1.** Baseline simulation parameters of different layers, used for simulating WSe$_2$-based dualjunction bifacial thin film solar cells [45, 46, 47].

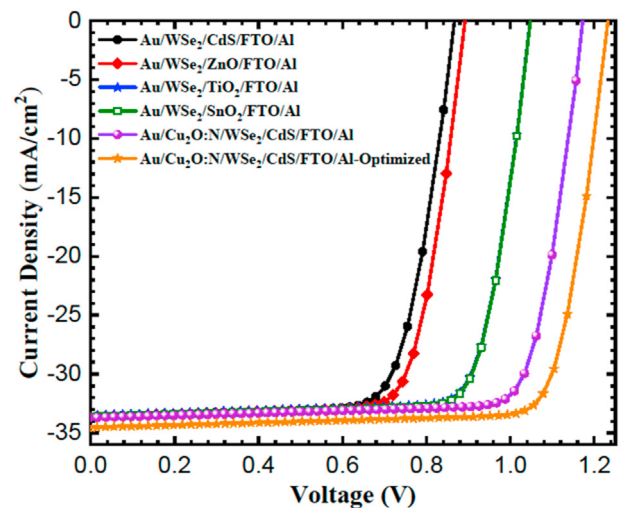| Parameters | FTO | TiO$_2$ | CdS | ZnO | SnO$_2$ | c-WSe$_2$ | Cu$_2$O:N |
|---|---|---|---|---|---|---|---|
| Layer type | Window | ETL | ETL | ETL | ETL | Absorber | BSF |
| Conductivity type | n | n | n | n | n | p | p$^+$ |
| Thickness (nm) | 50 | 100 | 100 | 100 | 100 | 1000 | 100 |
| Bandgap E$_g$ (eV) | 3.72 | 3.26 [48] | 2.42 | 3.31 | 3.6 [49] | 1.55 [50] | 2.6 [51, 52, 53] |
| Electron affinity, $\chi$ (eV) | 4.0 | 4.20 [48] | 4.30 | 4.35 | 3.93 [49] | 4.03 [54] | 3.2 |
| Relative permittivity $\varepsilon_r$ | 9.0 | 10.0 | 9.35 | 9.0 | 8.0 | 13.8 | 6.6 |
| Effective DOS at CB N$_C$ (cm$^{-3}$) | 2.2×10$^{19}$ | 2.2×10$^{18}$ | 2.2×10$^{18}$ | 2.2×10$^{18}$ | 3.16×10$^{18}$ [55] | 8.3×10$^{18}$ [56] | 2.5×10$^{20}$ |
| Effective DOS at VB N$_V$ (cm$^{-3}$) | 1.8×10$^{18}$ | 1.8×10$^{19}$ | 1.8×10$^{19}$ | 1.8×10$^{19}$ | 2.5×10$^{19}$ [55] | 1.4×10$^{19}$ [56] | 2.5×10$^{20}$ |
| Electron thermal velocity (cms$^{-1}$) | 10$^7$ | 10$^7$ | 10$^7$ | 10$^7$ | 10$^7$ | 1.7×10$^7$ [56] | 10$^7$ |
| Hole thermal velocity (cms$^{-1}$) | 10$^7$ | 10$^7$ | 10$^7$ | 10$^7$ | 10$^7$ | 1.4×10$^7$ [56] | 10$^7$ |
| Electron mobility, $\mu_n$ (cm$^2 V^{-1} s^{-1}$) | 20 | 0.1 [57] | 100 | 100 | 15 [58] | 30 [50] | 0.1 [53] |
| Hole mobility, $\mu_p$ (cm$^2 V^{-1} s^{-1}$) | 10 | 0.1 [57] | 25 | 25 | 0.1 [58] | 30 [50] | 0.1 [53] |
| Donor concentration, N$_D$ (cm$^{-3}$) | 1019 | 1018 | 1.15×10$^{17}$ | 1018 | 10$^{19}$ [58] | 0.0 | 0.0 |
| Acceptor concentration, N$_A$ (cm$^{-3}$) | 0.0 | 0.0 | 0.0 | 0.0 | 0.0 | 10$^{16}$ | 10$^{19}$ |
| Defect type | Acceptor | Acceptor | Acceptor | Acceptor | Acceptor | Donor | Donor |
| Energetic distribution | Gaussian | Gaussian | Gaussian | Gaussian | Gaussian | Gaussian | Gaussian |
| Peak defect density, N$_t$ (eV$^{-1}$cm$^{-3}$) | 1015 | 1016 | 2.5×10$^{17}$ | 10$^{16}$ | 10$^{16}$ | 10$^{14}$ | 10$^{15}$ |
| Characteristic energy (eV) | 0.1 | 0.1 | 0.1 | 0.19 | 0.1 | 0.1 | 0.1 |
| Reference energy (eV) | 0.6 | 0.6 | 0.6 | 0.6 | 0.6 | 0.6 | 0.6 |
| $\sigma_n$ for acceptor defect (cm$^2$) | 10$^{-15}$ | 10$^{-15}$ | 10$^{-15}$ | 10$^{-15}$ | 10$^{-15}$ | – | – |
| $\sigma_p$ for acceptor defect (cm$^2$) | 10$^{-15}$ | 10$^{-15}$ | 10$^{-15}$ | 10$^{-15}$ | 10$^{-15}$ | – | – |
| $\sigma_n$ for donor defect (cm$^2$) | – | – | – | – | – | 3.67 × 10$^{-14}$ | 10$^{-15}$ |
| $\sigma_p$ for donor defect (cm$^2$) | – | – | – | – | – | 4.46 × 10$^{-14}$ | 10$^{-15}$ |
| n$_t$ at WSe$_2$/ETL interface (cm$^{-2}$) | 1.0×10$^{16}$ | 1.0×10$^{16}$ | 1.0×10$^{16}$ | 1.0×10$^{16}$ | 1.0×10$^{16}$ | – | – |
| n$_t$ at HTL/WSe$_2$ interface (cm$^{-2}$) | – | – | – | – | – | – | 1.0×10$^{16a}$ |

[a] N.B.: DOS = Density of states, CB = Conduction band, VB = Valance band, $\sigma_n$ = Electron capture cross-section of defects, $\sigma_p$ = Hole capture cross-section of defects, $n_t$ = Defect density.

**Table 2.** Front and back contact parameters used in simulation.

| Parameters | Back-contact | Front-contact |
|---|---|---|
| Surface recombination velocity of electrons (cms$^{-1}$) | 1.0×10$^5$ | 1.0×10$^7$ |
| Surface recombination velocity of holes (cms$^{-1}$) | 1.0×10$^7$ | 1.0×10$^5$ |
| Work function (eV) | 5.47; Au (100) [59] | 4.06; Al [59] |
| Cell temperature (K) | 298–368 | |



**Figure 1.** J-V characteristics under front-illumination for the WSe$_2$-based heterojunction TFSCs with different ETLs and with Cu$_2$O:N HTL.

TCO and the absorber layer. Kessler J. et al. reported that SCs without ETL provide lower PCE compared to SCs with ETL [67]. Therefore, to implement the TFSC under high PCE conditions, the selection of the ETL is crucial. This section is devoted to a comprehensive study of the influence of different ETLs (namely CdS, ZnO, TiO$_2$, and SnO$_2$) and HTL on the PV performance of the WSe$_2$ SCs. Initially, the thickness of the WSe$_2$ layer and ETLs of all devices are fixed to 1000 nm and 100 nm, respectively. The other simulation parameters remain at the baseline values listed in Table 1.

Figure 1 exhibits the J-V characteristics curves of four WSe$_2$ devices having different ETLs. Simulation shows that the PCE produced by the WSe$_2$ device using CdS ETL is only 20.72%, which is far below the theoretical PCE limit for the WSe$_2$ SC with the absorption layer band gap of around 1.5 eV. Although the overall efficiency of the WSe$_2$/CdS device is not very high, it is expected to be the starting point for the WSe$_2$ SC to further enhance the device's performance. The device is then modified by replacing the CdS ETL with ZnO ETL. It is noteworthy that the performance of WSe$_2$ device with ZnO ETL is slightly improved. Compared with the device using CdS ETL, its PCE has increased by only about 8.6 % (the actual PCE is 22.68 %, which is within close range of the previously

reported results [43, 50]). The results are very promising, but due to carrier recombination, improper band structure, incomplete absorption, low carrier collection efficiency, etc., there are still losses, so it is very likely to further enrich the device's performance. For instance, the energy band structure at the WSe$_2$/ETL interface (see Figure 2) is still not optimal, which unfavorably affects the ($V_{OC}$) of the device. Therefore, other modifications will now be studied to help us get the efficiency of the device as close as possible to the Shockley-Queisser limit. TiO$_2$ is another commonly used ETL, which has been successfully employed in
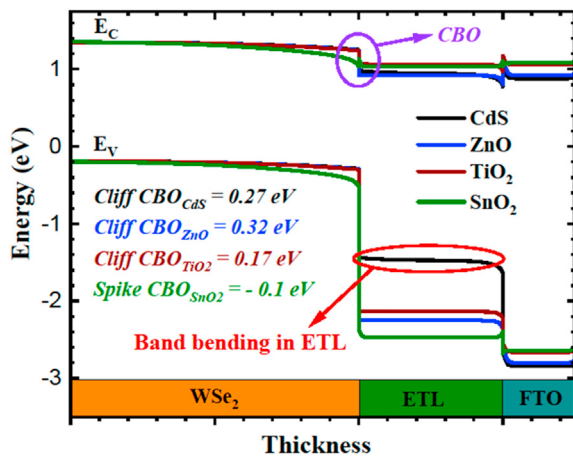
**Figure 2.** Energy levels of the WSe$_2$-based heterojunction TFSCs with different ETLs.

dye synthesis and perovskite SCs [68, 69]. Using TiO$_2$ as the ETL in the WSe$_2$ device, the $V_{OC}$ of the WSe$_2$ SC is 1.011 V, which is 177 mV higher than that of the CdS device, and the PCE is 26.43 %. However, deposition of TiO$_2$ is a high temperature (500 °C) process and it also suffers from intrinsic low electron mobility [70]. Alternatively, tin-oxide (SnO$_2$) with its earth-abundant compositions is a low-cost environment friendly, wide band gap n-type semiconductor with high and tunable carrier concentration [71], high electron mobility [72], low-temperature deposition process [73], high thermal and chemical stability, making them favourable ETL candidate for WSe$_2$ SCs. With SnO$_2$ as ETL, WSe$_2$ device has the best performance among other devices ($V_{OC}$ = 1.051 V, $J_{SC}$ = 33.30 mA/cm$^2$, FF = 77.56 % and PCE = 27.14 %).

Now we analyze the PV performance of the WSe$_2$/SnO$_2$ device with the incorporation of HTL. The specific HTL material to be studied in this work is Cu$_2$O:N. Wide band gap Cu$_2$O:N is a highly doped p-type semiconductor with the ability to allow the tuning of its acceptor

density [53], making it an appropriate HTL material for WSe$_2$ SCs. Figure 3 shows the device structure and energy band diagram of our proposed SLG/Au/Cu$_2$O:N/WSe$_2$/SnO$_2$/FTO/Al heterojunction TFSCs and its JV characteristics curve is also shown in Figure 1. When using Cu$_2$O:N as the HTL, the performance of the WSe$_2$/SnO$_2$ device is further improved: PCE = 29.46 %, $V_{OC}$ = 1.125 V, $J_{SC}$ = 33.60 mA/cm$^2$ and FF = 77.92%. The PV parameters of all WSe$_2$ devices are extracted from JV curves of the representative devices and listed in Table 3. The external quantum efficiency spectra of the WSe$_2$ SC with Cu$_2$O:N HTL and different ETLs are presented in Figure 4. A suitable quantum efficiency for all devices is obtained in the visible range and is related to the good current density ($\approx$33 mA/cm$^2$). For TiO$_2$ ETL, a drop in EQE at wavelength <400 nm is observed. However, the impact of Cu$_2$O:N HTL is clearly observed with improved EQE in the long-wavelength region, indicating that light-induced carrier generation and collection are improved. This drives to a further raise in the $J_{SC}$ ($\approx$34.0 mA/cm$^2$) of the device.

Defect states at the interface are formed due to large lattice mismatch, energy band misalignment, dangling bonds, surface defects, etc. Photo-generated carriers tend to occupy and then recombine with these defect states, thereby hindering the PV performance of the SCs. There are two types of energy band structures at the absorber/ETL interface, namely *cliff-like* ($E_{C(ETL)} < E_{C(abs.)}$) and *spike-like* ($E_{C(ETL)} > E_{C(abs.)}$) [74]. The activation energy ($E_a$) of carrier recombination at the interface depends on the energy band structure at the absorber/ETL interface. The higher the $E_a$, the lower the interface recombination, and vice-versa [75, 76]. For the *cliff-like* band structure, the $E_a$ ($E_a = E_{g(abs)} - CBO$) is smaller than the band gap of the absorber layer, which leads to an increase in interface recombination of minority carriers, thereby reducing the $V_{OC}$ of the SC. The opposite is true for the *spike-like* band structure at the absorber/ETL interface.

T. Minemoto et. al showed that the *spike-like* band structure at the absorber/ETL interface with CBO of 0 to - 0.4 eV is beneficial for high-performance SCs [77]. The energy band structure of WSe$_2$ SCs with different ETLs is shown in Figure 2. It is observed that a *cliff-like* band structure with $CBO$ = 0.27 eV is developed at the WSe$_2$/CdS interface,
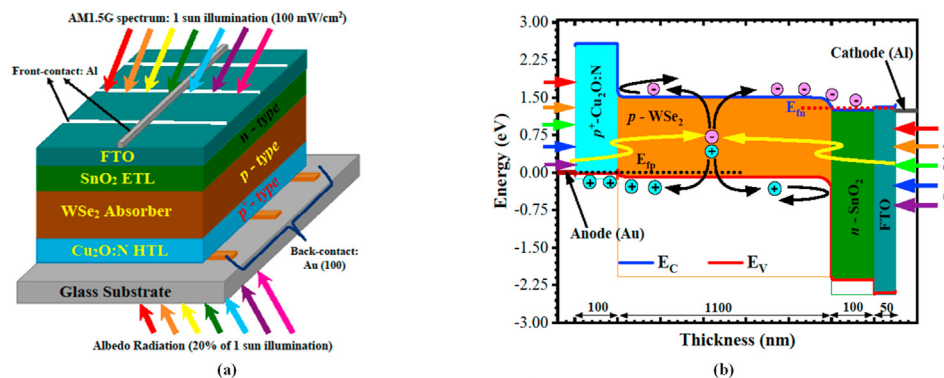


**Figure 3.** (a) Schematic of the proposed bifacial dual-junction WSe$_2$ solar cell and (b) it's energy band diagram.

**Table 3.** PV performance parameters of WSe$_2$ solar cells with HTL and different ETLs.

| ETL | HTL | $V_{OC}$ (Volt) | $J_{SC}$ (mA/cm$^2$) | FF (%) | PCE (%) | *$K_T$ | Cell Configuration |
|-----|-----|-----|-----|-----|-----|-----|-----|
| CdS | – | 0.847 | 33.41 | 73.21 | 20.72 | 2.89 | Au/WSe$_2$/CdS/FTO/Al |
| ZnO | – | 0.894 | 33.47 | 75.75 | 22.68 | 2.25 | Au/WSe$_2$/ZnO/FTO/Al |
| TiO$_2$ | – | 1.024 | 33.40 | 77.28 | 26.43 | 2.29 | Au/WSe$_2$/TiO$_2$/FTO/Al |
| SnO$_2$ | – | 1.051 | 33.30 | 77.56 | 27.14 | 2.30 | Au/WSe$_2$/SnO$_2$/FTO/Al |
| SnO$_2$ | Cu$_2$O:N | 1.125 | 33.60 | 77.92 | 29.46 | 1.64 | Au/Cu$_2$O:N/WSe$_2$/SnO$_2$/FTO/Al |
| SnO$_2$ | Cu$_2$O:N | 1.25 | 33.92 | 79.88 | 33.84 | 1.64 | Au/Cu$_2$O:N/WSe$_2$/SnO$_2$/FTO/Al** |

*$K_T$ is the temperature coefficient of $P_{max}$ and expressed in parts per thousand and Kelvin.

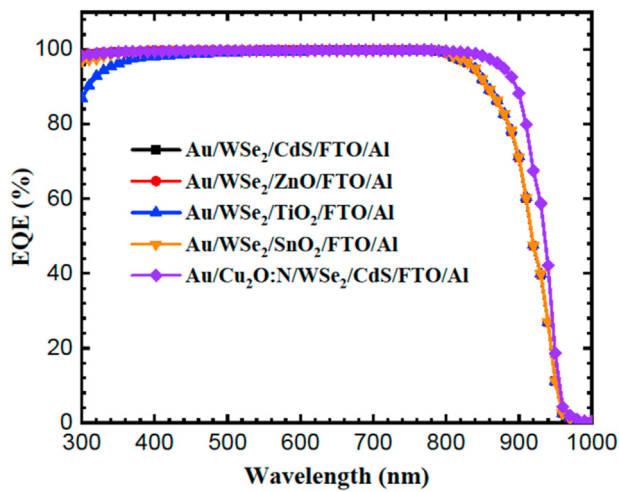**After optimization of thickness and carrier concentration of different layers.

**Figure 4.** EQE spectra of the WSe$_2$-based heterojunction TFSCs with HTL and different ETLs.

which enhances the minority carrier recombination, as shown by Figure 5, and thereby reducing the $V_{OC}$ of the device, as shown by the JV curve in Figure 1 and in Table 3. Another important attribute of the band structure at the WSe$_2$/CdS interface is that the band bending also occurs in the CdS region, which indicates that most of the interface defect states are occupied by acceptor defects [78]. Therefore, the Fermi level is pinned at the intermediate gap area and restricts the quasi-Fermi levels splitting under illumination and results in a poor $V_{OC}$ at the cell output. In addition, the very high lattice mismatch (24.5 %, see Table 4) at the WSe$_2$/CdS interface would further deteriorate the device performance. Therefore, we conclude that CdS ETL is not suitable for high-performance WSe$_2$ SCs.
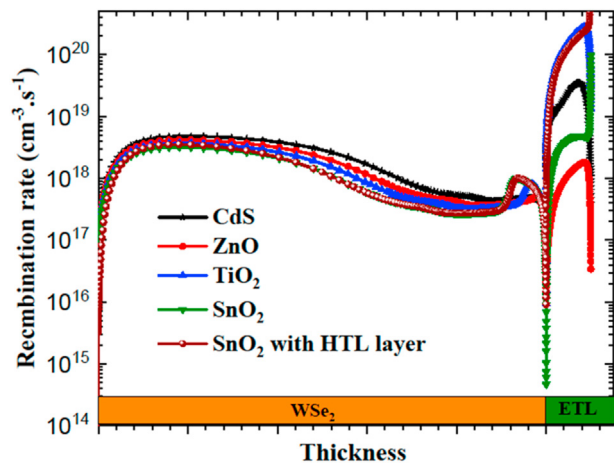


**Figure 5.** Recombination rate of the WSe$_2$-based heterojunction TFSCs with HTL and different ETLs.

**Table 4.** Lattice mismatch* at WSe$_2$/ETL interface with different ETLs.

| Layer | Lattice Parameters | | | Lattice Mismatch |
|---|---|---|---|---|
| | a (Å) | b (Å) | c (Å) | |
| WSe$_2$ | 3.25 | 3.25 | 12.97 | – |
| CdS | 4.16 | 4.16 | 6.756 | 24.56 % |
| ZnO | 3.249 | 3.249 | 5.205 | 0.03 % |
| TiO$_2$ | 4.594 | 4.594 | 2.958 | 9.40 % |
| SnO$_2$ | 4.737 | 4.737 | 3.186 | 2.0 % |

*$\delta = 2|a_s - a_e|/(a_s + a_e)$

Although the *cliff-like CBO* at the WSe$_2$/ZnO interface is somewhat higher than that at the WSe$_2$/CdS interface, the slight improvement of the PCE of the WSe$_2$ device with ZnO ETL (see Table 3) may be associated with the reduction in carrier recombination due to nearly perfect lattice matching at the WSe$_2$/ZnO interface (see Table 4) [79] as compared to the WSe$_2$/CdS interface, low absorption of light below 500 nm by the ZnO layer and reduced series resistance of WSe$_2$/ZnO device (as the FF increased). The band structure at the WSe$_2$/TiO$_2$ interface shows a *cliff-like CBO* of 0.17 eV, which is significantly lower than the first two devices. As a matter of fact, due to the reduction of minority carrier recombination, as witnessed in Figure 5, the PCE of the WSe$_2$/TiO$_2$ device further increased to 26.43 %, see Table 3.

According to our simulated results, the SnO$_2$ ETL produces the highest PCE compared to other ETLs. When SnO$_2$ is used as ETL, the conduction band (- 3.93 eV) of SnO$_2$ is higher in potential than WSe$_2$ layer (- 4.03 eV), resulting in the set-up of a small *spike-like CBO* of - 0.1 eV at the WSe$_2$/SnO$_2$ interface, which helps to prevent minority carriers from recombining at this interface. Therefore, this improved performance of the WSe$_2$/SnO$_2$ device is due to favourable band alignment at the WSe$_2$/SnO$_2$ interface, extended depletion layer width (see Figure 6), high carrier mobility of SnO$_2$ ETL; this significantly improve carrier collection, and good lattice matching (only 2.0 % lattice mismatch, see Table 4), at the WSe$_2$/SnO$_2$ interface. Another important parameter is the field generated at the WSe$_2$/ETL interface, which affects the injection of photogenerated electrons from the absorber layer to the ETL. Figure 6 shows the electric field at the WSe$_2$/ETL interface for different ETLs. It can be seen that the field generated by CdS, ZnO, and TiO$_2$ TELs at the WSe$_2$/ETL interface is relatively poor. However, SnO$_2$ ETL exhibits an improved field at the interface, which forces to separate photogenerated electron-hole pairs and effectively collects electrons from the absorber layer. With the understanding of device performance improvement, we chose SnO$_2$ as ETL for the WSe$_2$ SC to carry on further study.

By using Cu$_2$O:N HTL, the field at the Cu$_2$O:N/WSe$_2$ interface enhances the potential distribution along the absorber layer, as it is noticed in Figure 6, which reduces carrier recombination in the bulk absorber layer as well as at the interfaces, as viewed in Figure 5, and improved the $V_{OC}$. This field also enhances the separation and collection of photo-induced carriers at the electrode, thereby also increasing $J_{SC}$.

### 3.2. Device optimization

#### 3.2.1. Effect of absorber layer thickness and carrier concentration

In this section, the final device structure of SLG/Au/Cu$_2$O:N/WSe$_2$/SnO$_2$/FTO/Al is optimized for the highest PCE in terms of thickness and carrier concentration of all layers. In TFSCs, most of carrier generation by incident photons occurs in the absorber layer. Minority carrier recombination also occurs in the absorber layer. Therefore, thickness of the
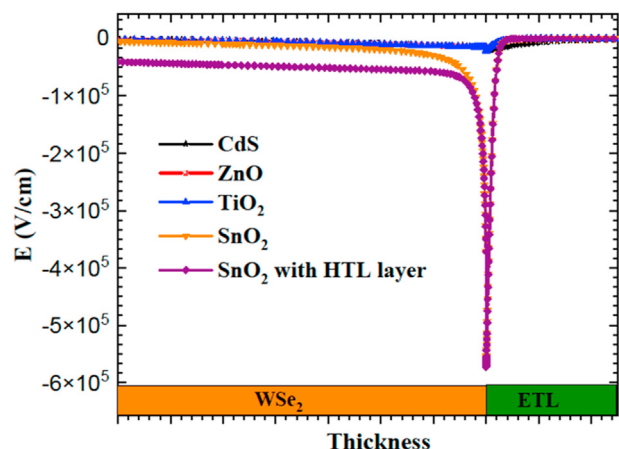


**Figure 6.** Electric field at the WSe$_2$/ETL interface with HTL and different ETLs.

active layer of SC is an influential parameter to obtain the best performance, as the diffusion length of free carriers represents a constraint with the thickness. To study the influence of the absorber's thickness, simulation was executed by changing it from 300 nm to 2000 nm and putting up all other input parameters at the baseline values summarized in Table 1. Figure 7 illustrates the effect of absorber layer thickness on the PV performance of the WSe$_2$ SC. Because of less carrier recombination in the bulk region of the absorber layer, the photogenerated current ($J_{SC}$) is lower and the charge extraction rate is higher for the thin absorber layer, as evidenced by the high $V_{OC}$, shown in Figure 7(a). As the thickness increases from 300 nm to 1100 nm, the $J_{SC}$ sharply increases from ≈30.45 mA/cm$^2$ to ≈33.8 mA/cm$^2$ and then slowly increases until all photons are absorbed, and finally saturated to ≈34.40 mA/cm$^2$. In contrast to $J_{SC}$, $V_{OC}$ of the device decreases from 1.16 to 1.12 V as the thickness increases from 300 to 1100 nm, and the $V_{OC}$ decreases at a slower rate exceeding this thickness. PCE and FF follow the same trend of $J_{SC}$ up to the thickness of 1650 nm and then reduce at a diminishing rate as the thickness further increases.

The $J_{SC}$ is lower for the thinner absorber layer (<1000 nm), which is due to the lower absorption of light by the absorber layer [80]. Nevertheless, the effective band gap of semiconductor thin films decreases as its thickness increases [81] and thereby increases $J_{SC}$. However, carrier recombination in the bulk region of the WSe$_2$ layer increases when its thickness is comparable with the diffusion length of the free carriers, and as a result, $V_{OC}$ decreases. Therefore, in order to operate SCs under high-performance conditions, tuning of absorber layer thickness is essential to maximize current density and minimize bulk recombination. At this point, the best performance was found at the absorber layer thickness of 1650 nm for the monofacial WSe$_2$ SC.

Figure 8 shows the variation of key PV parameters of the WSe$_2$ SC for various acceptor densities of the WSe$_2$ layer ranging from $10^{15}$ to $10^{19}$ cm$^{-3}$. It can be seen that, except for $J_{SC}$, all PV parameters show a similar trend of exponential growth with the acceptor density up to $2 \times 10^{18}$ cm$^{-3}$ and then severely reduced with further increase of acceptor density. When the acceptor density in the absorber layer increases, the built-in potential at the junction of the SC also increases, which forces the charge carriers to move to the corresponding electrodes and enhances the collection of photoinduced carriers and thus, the cell efficiency. FF also increases with the increase of the acceptor level, up to $2 \times 10^{18}$ cm$^{-3}$, which is because of increasing in the conductivity of the WSe$_2$ layer. Beyond this value of acceptor concentration, a negative effect on FF is observed. On the contrary, $J_{SC}$ decreases with increasing the acceptor concentration. When the acceptor concentration in active layer of SC increases, it incompatibly affects the carrier mobility and enhances the inter-band recombination of photo-induced carriers, resulting in the insufficient carrier collection. In addition, Auger recombination and impurity scattering in the absorber layer may play a significant role
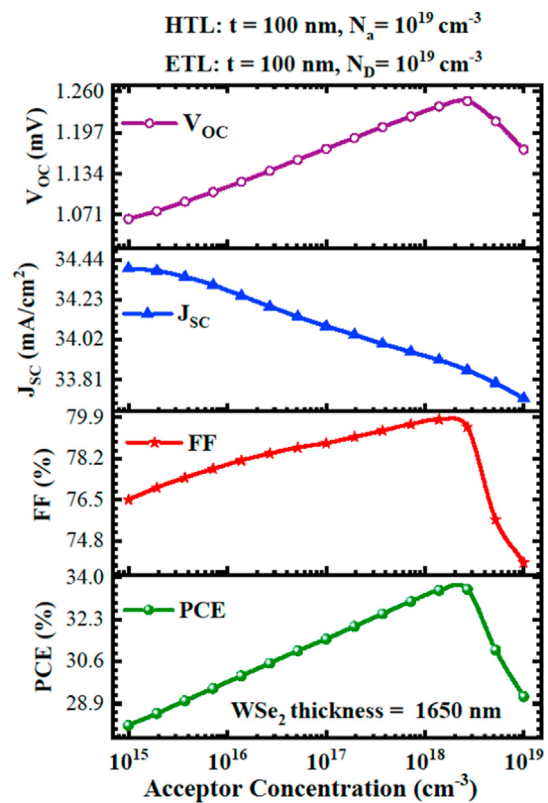


**Figure 8.** Key PV parameters of the WSe$_2$ solar cell as a function of acceptor concentration of the absorber layer.

under high carrier density, resulting in a decrease in $J_{SC}$. The best performance is obtained when the acceptor concentration is around $2 \times 10^{18}$ cm$^{-3}$. This optimized carrier density for the absorber layer enhanced the PCE to 33.6 % from an unoptimized PCE of 29.8 % for the WSe$_2$ SC.

### 3.2.2. Effect of carrier concentration of SnO$_2$ ETL and Cu$_2$O:N HTL on the device performance

In this section, the carrier concentrations of ETL and HTL are optimized for the highest PCE, using the previously obtained optimized values of absorber layer thickness and acceptor density. Our results show that within the thickness of around 50–150 nm for both HTL and ETL layers, the device performance does not change too much. Therefore, considering simulated results and the fabrication cost, the optimal thickness of 100 nm was chosen for both layers. It has become obvious
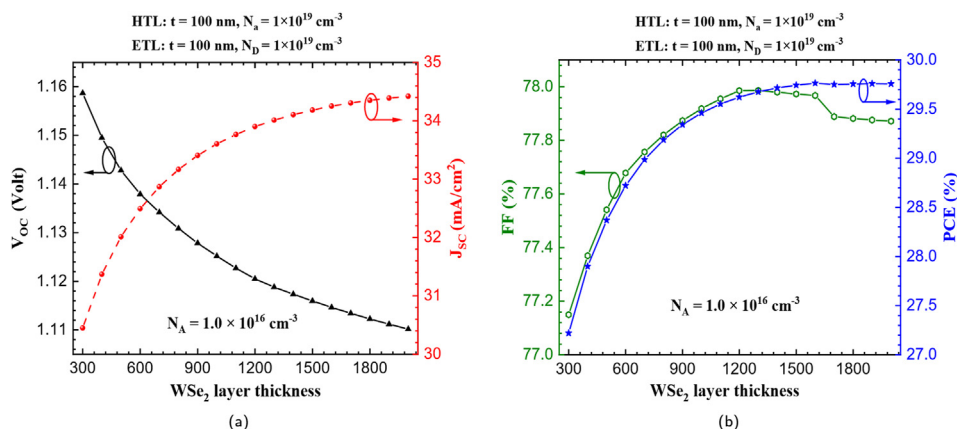


**Figure 7.** Influence of the WSe$_2$ layer thickness on PV performance parameters: (a) $V_{OC}$ and $J_{SC}$ and (b) FF and PCE.

that this thickness is adequate for the high efficiency of the WSe$_2$ SC. To study the effect of HTL carrier concentration, it was changed from $10^{17}$ cm$^{-3}$–$10^{21}$ cm$^{-3}$ and the results are displayed in Figure 9(a). As shown in Figure 9(a), $V_{OC}$ is constant and independent of carrier concentration, which indicates that there are very few minority carriers in the HTL as photogenerated electrons in the absorber layer are effectively blocked by the sufficiently high potential formed by the high CBO at the HTL/WSe$_2$ interface, see Figure 3(b). This finding also confirms that due to favorable band alignment at the HTL/absorber interface, Cu$_2$O:N HTL effectively blocks electrons and only accepts holes from the absorber [82] (see Figure 3(b)). Between lightly-doped and highly-doped HTL, the main differences in cell performance are the $J_{SC}$ and FF. As the carrier density of HTL increases, the FF improves initially, which is due to an improvement in conductivity and sheet resistance of HTL [83]. Our results show that when the carrier density of HTL is $3.5 \times 10^{19}$ cm$^{-3}$, the $V_{OC}$, $J_{SC}$, and FF of the device are 1.244 V, 33.92 mA/cm$^2$, and 79.8 % respectively and an eminent PCE of 33.67 % is obtained. The response of the proposed WSe$_2$ SC is also analyzed based on changing the ETL donor density from $10^{17}$ to $10^{20}$ cm$^{-3}$. The influence of ETL donor density on cell performance parameters is shown in Figure 9(b). It is evident that $J_{SC}$ maintains nearly identical value with the variation of ETL donor density. On the other hand, the values of $V_{OC}$, FF, and PCE begin to increase at a slow rate between $10^{17}$ cm$^{-3}$ to $2 \times 10^{18}$ cm$^{-3}$ and increase sharply from $2 \times 10^{18}$ cm$^{-3}$ to $10^{19}$ cm$^{-3}$ and finally saturate beyond that donor level. The optimum value chosen for ETL donor density is $3.75 \times 10^{19}$ cm$^{-3}$ on which the PCE of SC reached a value of 33.84 % with $V_{OC}$, $J_{SC}$, and FF of 1.25 V, 33.92 mA/cm$^2$, and 79.88 % respectively.

### 3.3. Effect of cell temperature on the performance of WSe$_2$ solar cells

Environmental parameters strongly affect the overall PV performance of TFSCs. The cell temperature is recognized to be a key environmental parameter that determines SC performance and quality. Since the typical operating temperature of the SC is about 45 °C ± 2 °C, observations are made in the range of 298 K–368 K with a step of 10 K. The temperature coefficient of $P_{max}$ ($K_T$) is an indicator of performance of PV devices, shows how higher operating temperature affects the device's performance. It can be expressed as follows [84]:

$$K_T = \frac{1}{P_{\max(STC)}} \frac{dP_{max}}{dT} \qquad (1)$$

where, $P_{max(STC)} = V_{mpp} \times J_{mpp}$ under standard test conditions (298 K); $V_{mpp}$ and $J_{mpp}$ are the voltage and current density at the maximum power point of the JV curve, respectively. Using Eq. (1), $K_T$, the temperature coefficient of $P_{max}$ for all WSe$_2$ devices studied herein are calculated and tabulated in Table 3. From the data in Table 3, it can be seen that the WSe$_2$ device with SnO$_2$ ETL and Cu$_2$O: N HTL exhibits $K_T = -1.64$ (parts per thousand and Kelvin), indicating the best thermal stability among all WSe$_2$ devices studied herein and is better than previously reported results [84]. It is because of low temperature coefficient of energy bandgap ($E_g$) of WSe$_2$ thin films [12].

The J-V characteristics of the optimized WSe$_2$ SC with SnO$_2$ ETL and Cu$_2$O:N HTL at different cell temperature are presented in Figure 10(a). The cell temperature was varied from 25 °C to 95 °C with a step of 10 °C. It is clearly seen in Figure 10(a) that the cell temperature has a significant impact on the J-V characteristics of the WSe$_2$ SC. Normalized PV parameters ($V_{OC}$, $J_{SC}$, FF, and PCE) extracted from J-V curves as function of cell temperature are illustrated in Figure 10(b). As seen in Figure 10(b) that the FF and $V_{OC}$ decrease while the $J_{SC}$ increases slightly with cell temperature. It is also noticed that the $V_{OC}$ strongly depends on cell temperature, whereas, the $J_{SC}$ shows only slight variation. The observed impact of cell temperature on $V_{OC}$ can be interpreted by the temperature-dependent built-in potential at the *pn* junction of the SC. The intrinsic carrier concentration in the semiconductor increases, as the cell temperature increases. Therefore, when cell temperature increases, the built-in potential of the *pn* junction decreases, which lead to a decrease in $V_{OC}$ of the device. On the other side, the carrier generation rate in semiconductors increases with increase in the cell temperature, which causes the $J_{SC}$ to increase [85]. A similar result is also observed in earlier reported works [86, 87].

### 3.4. Bifacial WSe$_2$ solar cells

Compared with traditional monofacial SCs, the energy harvest per unit area of SCs can be increased without significantly increasing the manufacturing complexity and cost by utilizing bifacial concept. Recent
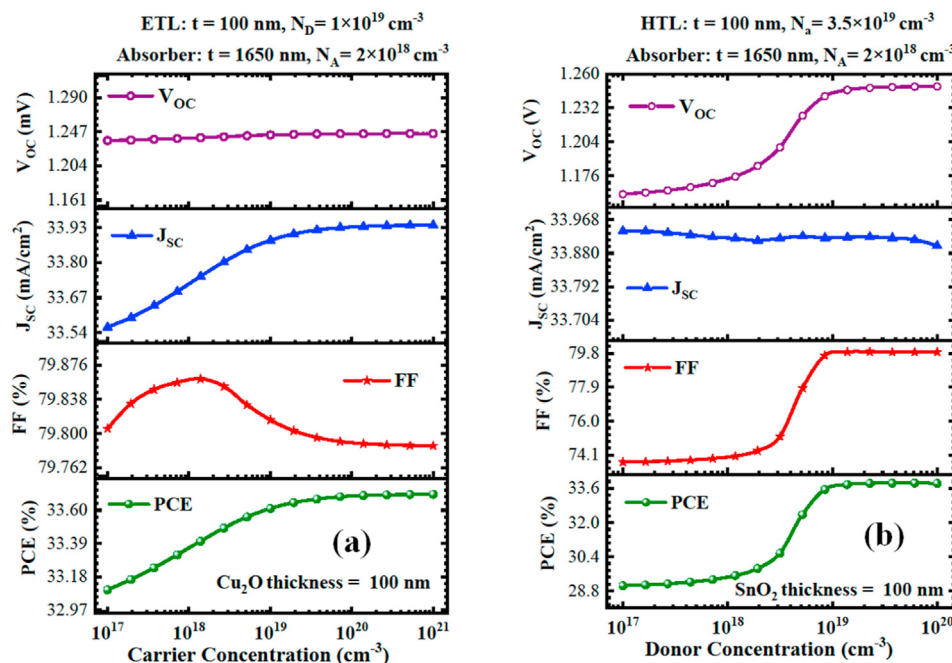
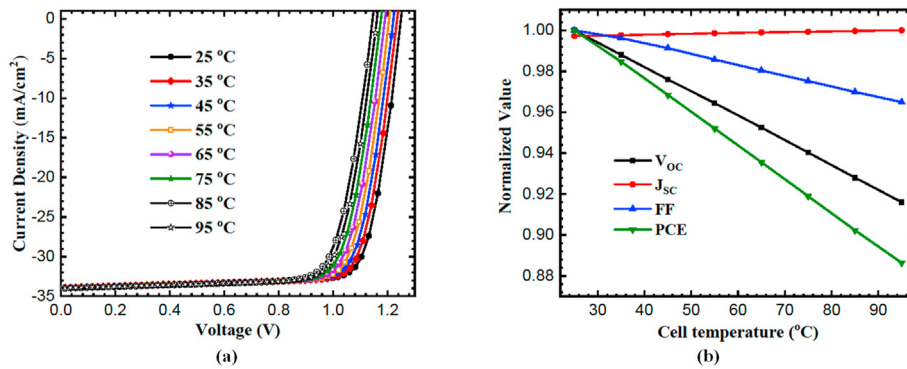**Figure 9.** Variation of cell performance as a function of (a) HTL (b) ETL carrier concentration.

**Figure 10.** (a) The J–V characteristics (b) Variation of normalized values of PV parameters of the WSe$_2$ solar cell with different cell temperature.

studies have shown that, compared with monofacial SCs, the bifacial SCs installed under high albedo surface can increase the energy at the output to 20–30% [88, 89]. Based on these advantages, the International Photovoltaic Technology Roadmap (ITRPV) predicts that by 2028, bifacial SCs will account for about 40% of the world PV market share [90].

The key parameters that govern the back side contribution of bifacial SCs are the back surface absorption loss, diffusion length of minority carrier, minority carrier lifetime, absorber layer thickness, albedo coefficient of background surface, etc. In a conventional monofacial SC, the front surface with a metallic grid pattern is transparent to allow maximum light to enter the absorber layer. However, an opaque metal film is coated on the back side of the monofacial SC. In contrast, the metallic grid pattern is deposited on both surfaces of the bifacial SC, as demonstrated in Figure 3(a), to reduce surface recombination velocity and material costs, and HTL material with high acceptor density and optical transparency is used to admit maximum photons from back surfaces. In our proposed WSe$_2$ SC, the advantage of using Cu$_2$O:N HTL is the possibility of designing bifacial SCs by allowing maximum collection of albedo components. The use of Cu$_2$O:N HTL at the rare side of the WSe$_2$ SCs can be justified by their high acceptor density and high optical transparency in the visible region [91, 92]. The relation between the diffusion length and the lifetime of free carriers is as follows:

$$L_d = \sqrt{\frac{KT}{q}} \cdot \sqrt{\mu\tau} \qquad (2)$$

where, $KT/q$ is the thermal voltage (0.02586 V at 300 K), $\mu$ is the mobility of the carrier in the c-WSe$_2$ thin films (30 cm$^2$ V$^{-1}$s$^{-1}$ [50]). According to earlier reports, the lifetime ($\tau$) of minority carriers in the c-WSe$_2$ film is around 30 ns [60, 61]. Using this Eq. (2), the diffusion length of free carriers in the c-WSe$_2$ thin-film is estimated to be greater than 1200 nm. Therefore, due to the elongated diffusion length and carrier lifetime in the c-WSe$_2$ film, if the thickness of the WSe$_2$ layer is less than 1200 nm, regardless of the direction of the incident light, the photogenerated carriers can reach the corresponding electrode before recombination.

For bifacial SCs, the simulation is quite complicated due to the additional illumination from the back side. For bifacial SCs, PV parameters are usually calculated using independent measurements for both back and front side illumination under one sun conditions [93]. Therefore, we present a simulation method for the bifacial SCs, which divides our computations into two independent simulations of the rare and front side illumination of the device. Herein, we use the terms bifacial factor (BF) and bifacial gain (BG) to understand the asymmetric photoelectric behaviour of bifacial devices. The BF is defined by Eq. (3) and allows to estimate the relative response of each side of the device when illuminated individually.

$$BF = \frac{X_{back}}{X_{front}} \qquad (3)$$

where, $X$ is any PV parameter ($V_{OC}$, $J_{SC}$, FF or PCE) of the device under front, and back illumination condition.

The value of the albedo coefficient depends on the reflection characteristics of the surface. In the range of 300 nm–1300 nm, the integrated average of the spectral albedo coefficients of different surfaces varies from 15.0 % to 88 % [94]. In this simulation, in order to provide some insights, we considered that the WSe$_2$ device was running on a background surface with a 20 % albedo coefficient, and added the relative efficiencies of front and back illumination to calculate the bifacial efficiency: $\eta_{bi} = \eta_{front}$ *(at 1 sun)* $+ \eta_{back}$ *(at 20% of 1 sun)*. The additional contribution of the back side illumination to the PCE of the device is represented by BG and defined by Eq. (4) as follows:

$$BG_\eta = \frac{\eta_{bi} - \eta_{front}}{\eta_{front}} \qquad (4)$$

The bifacial SC allows photons to enter into the absorber layer from either side of the device. Therefore, the absorber layer thickness is an important parameter to achieve the best performance of bifacial SCs. The WSe$_2$ absorber thickness was varied between 300 nm and 2000 nm in order to find the optimum PCE condition for the bifacial SCs. The dependence of the PV parameters on the thickness of WSe$_2$ layer for both back and front illumination conditions (1 sun) is presented in Figure 11. For the front and back illumination conditions, as the WSe$_2$ layer thickness increases, the $V_{OC}$ of the device gradually decreases, as viewed in Figure 11(a) and the FF slightly increases (FF not shown). However, as the WSe$_2$ layer thickness increases, $J_{SC}$ as well as PCE exhibit the same behaviour under both illumination conditions. In particular, $J_{SC}$ and PCE increase sharply with the thickness of the WSe$_2$ layer up to 800 nm under both back and front illumination condition and then, on further increasing WSe$_2$ layer thickness, both of these PV parameters start decreasing gradually for back-illuminated device and continue increasing at a slow rate and finally saturate for the front-illuminated device, as manifested in Figures 11(b) and 11(c).

Under back-illuminated conditions, when the thickness of the WSe$_2$ layer is comparable with the diffusion length of the minority carriers, the bulk and back contact recombination will be higher, because more minority carriers reach the back contact and recombine. Therefore, we have optimized the thickness of the WSe$_2$ layer for the best efficiency condition in bifacial mode. The optimal WSe$_2$ layer thickness for this particular WSe$_2$ bifacial device is 1100 nm. Note that as mentioned earlier, the optimized WSe$_2$ layer thickness of the monofacial WSe$_2$ is 1650 nm. Therefore, relatively thin WSe$_2$ bifacial devices perform better than thicker devices. These findings are in agreement with previously reported results [95].

J-V characteristics curves of the WSe$_2$ SC with this optimized absorber layer thickness under front illumination at 1 sun, back-illumination at 1 sun, and back-illumination at 20 % of 1 sun conditions are shown in Figure 12. The overall PV performance of the WSe$_2$ SC is lower at the back illumination condition than that at the front-illumination condition.

Using Eq. (3), We observe that the BF of $V_{OC}$ and FF maintain values of 99.59 % and 100 %, respectively, indicating that there are no additional losses that may be involved when the device is illuminated from the back.
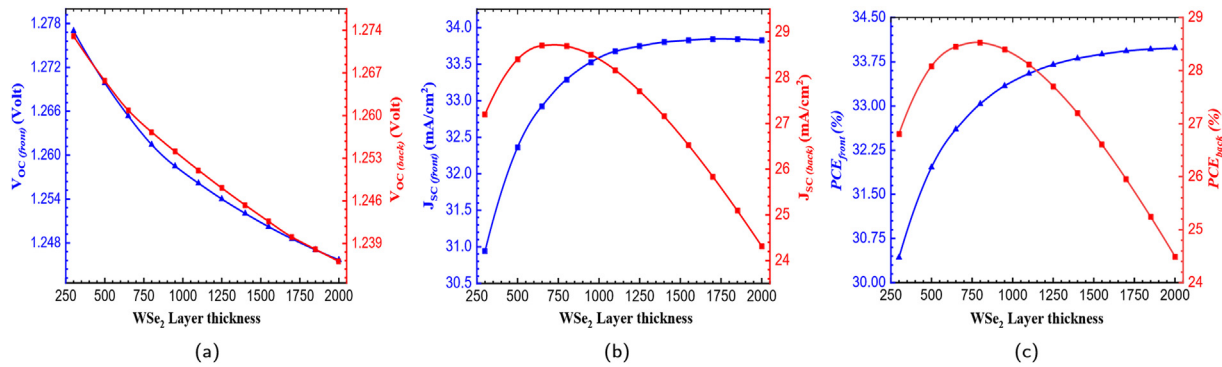
**Figure 11.** Dependence of PV parameters (a) $V_{OC}$ (b) $J_{SC}$ and (c) PCE of the WSe$_2$ solar cell on the absorber layer thickness for front- and back-side illumination (1 sun).
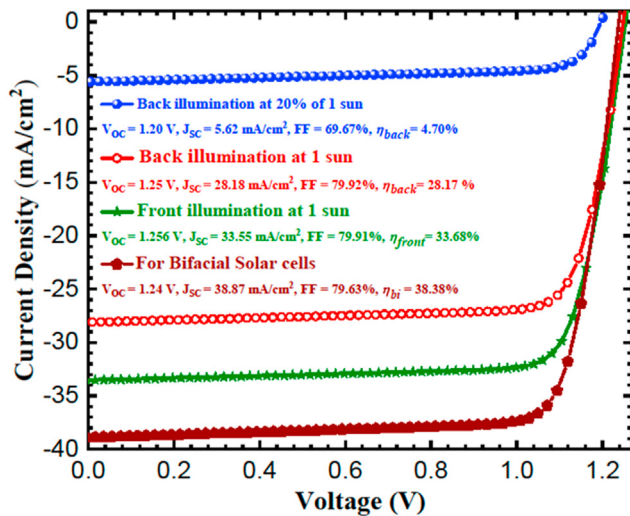


**Figure 12.** JV characteristics curves of the WSe$_2$ solar cell under front illumination at 1 sun, back-illumination at 1 sun, back-illumination at 20 % of 1 sun conditions, and net JV curve for bifacial WSe$_2$ solar cells.

The BF for $J_{SC}$ is around 84 %, which is due to significant absorption loss at the back surface of the WSe$_2$ device. As a result, it is found that the BF of the PCE of the WSe$_2$ device is 83.64 %. According to the JV characteristics in Figure 12, the WSe$_2$ device provides a PCE of 33.68 % and 4.70 % under front illumination at 1 sun and back illumination at 20% of 1 sun, respectively. Hence our simulation predicts that the bifacial PCE ($\eta_{bi}$) of the WSe$_2$ device is 38.38 %. Using Eq. (4), the bifacial gain (BG) of the WSe$_2$ device is estimated to be 13.95 %. The findings of this investigations are in agreement with previously reported results [88, 89].

## 4. Conclusions

In this work, SCAPS-1D was used to model a low-cost, environmentally friendly, earth-abundant tungsten diselenide (WSe$_2$)-based TFSC with Cu$_2$O:N HTL and various ETLs, namely CdS, ZnO, TiO$_2$ and SnO$_2$. First, the best ETL material for the WSe$_2$ SC (in terms of device performance) was determined from various ETLs, which was identified to be SnO$_2$. The suitability of SnO$_2$ ETL for the WSe$_2$ SC was demonstrated by proper lattice matching at the WSe$_2$/SnO$_2$ interface and appropriate band alignment between the conduction bands of SnO$_2$ and WSe$_2$. This study showed that the minority carrier recombination in the bulk region of the absorber layer and at the back-contact reduced significantly when the device was pulled off by adding a heavily doped thin (100 nm) Cu$_2$O:N layer between absorber and back electrode as HTL, which led to further improving the PV performance of the WSe$_2$/SnO$_2$ device. Several factors such as the thickness and carrier density of each layer of the device, the

operating temperature etc. affecting the device's performance were investigated. At optimized condition, the highest PCE of the monofacial WSe$_2$ SC was 33.84 % at the WSe$_2$, SnO$_2$ and Cu$_2$O:N layer thicknesses of 1650, 100 and 100 nm with the carrier concentrations of $2.0 \times 10^{18}$, $3.75 \times 10^{19}$, and $3.50 \times 10^{19}$ cm$^{-3}$, respectively. The effect of temperature on the PV performance of WSe$_2$-based SCs was also reported. The simulation was performed under the cell temperature range of 25–95 °C. The proposed WSe$_2$ device showed very good performance stability at high temperature, with a temperature coefficient of $P_{max}$, $K_T = -1.64$ (parts per thousand and Kelvin). In the present article, the proposed SLG/Ag/Cu$_2$O:N/WSe$_2$/SnO$_2$/FTO/Al device structure of the WSe$_2$ SC was also brought to use for the bifacial WSe$_2$ solar cell. We found that the performance of the WSe$_2$ device under the back-illuminated condition was slightly lower than that of the front-illuminated condition, and the BF of the PCE was about 84.0 %. The bifacial WSe$_2$ device with a relatively thin absorber layer performed better than the thick WSe$_2$ device. This investigation has revealed that the optimal thickness of the absorber layer for this particular bifacial WSe$_2$ device is 1100 nm. The bifacial WSe$_2$ device under simultaneous irradiation of 1 sun from the front side and 20.0 % of 1 sun from the back side provides improved PCE of 38.38 % with the BG of PCE is around 14 %. Therefore, this work could provide an insightful approach for designing and fabricating cost-effective, earth-abundant, environment friendly, efficient, and thermally stable bifacial WSe$_2$-based TFSCs.

## Acknowledgments

## References

[1] C.A. Wolden, J. Kurtin, J.B. Baxter, I. Repins, S.E. Shaheen, J.T. Torvik, A.A. Rockett, V.M. Fthenakis, E.S. Aydil, Photovoltaic manufacturing: present status, future prospects, and research needs, J. Vac. Sci. Technol. 29 (2011), 030801.

[2] A. Goetzberger, C. Hebling, H.-W. Schock, Photovoltaic materials, history, status and outlook, Mater. Sci. Eng. R Rep. 40 (2003) 1–46.

[3] National Renewable Energy Laboratory, Best Research-Cell Efficiency Chart, Technical Report, 2021 (Accessed: October 2021).

[4] M. Green, E. Dunlop, J. Hohl-Ebinger, M. Yoshita, N. Kopidakis, X. Hao, Solar cell efficiency tables (version 57), Prog. Photovoltaics Res. Appl. 29 (2020) 3–15.

[5] F. Alharbi, J.D. Bass, A. Salhi, A. Alyamani, H.-C. Kim, R.D. Miller, Abundant non-toxic materials for thin film solar cells: alternative to conventional materials, Renew. Energy 36 (2011) 2753–2758.

[6] M.A. Rahman, Design and simulation of a high-performance Cd-free $Cu_2SnSe_3$ solar cells with SnS electron-blocking hole transport layer and $TiO_2$ electron transport layer by SCAPS-1d, SN Appl. Sci. 3 (2021) 253.

[7] M.A. Rahman, Enhancing the photovoltaic performance of Cd-free $Cu_2ZnSnS_4$ heterojunction solar cells using SnS HTL and $TiO_2$ ETL, Sol. Energy 215 (2021) 64–76.

[8] F. El-Mellouhi, E.T. Bentria, S.N. Rashkeev, S. Kais, F.H. Alharbi, Enhancing intrinsic stability of hybrid perovskite solar cell by strong, yet balanced, electronic coupling, Sci. Rep. 6 (2016).

[9] K. Aitola, K. Domanski, J.-P. Correa-Baena, K. Sveinbjörnsson, M. Saliba, A. Abate, M. Grätzel, E. Kauppinen, E.M.J. Johansson, W. Tress, A. Hagfeldt, G. Boschloo, High temperature-stable perovskite solar cell based on low-cost carbon nanotube hole contact, Adv. Mater. 29 (2017), 1606398.

[10] X. Wang, L.-L. Deng, L.-Y. Wang, S.-M. Dai, Z. Xing, X.-X. Zhan, X.-Z. Lu, S.-Y. Xie, R.-B. Huang, L.-S. Zheng, Cerium oxide standing out as an electron transport layer for efficient and stable perovskite solar cells processed at low temperature, J. Mater. Chem. 5 (2017) 1706–1712.

[11] R. Frindt, The optical properties of single crystals of $WSe_2$ and $MoTe_2$, J. Phys. Chem. Solid. 24 (1963) 1107–1108.

[12] J.B. Goodenough, Band model for transition-metal chalcogenides having layer structures with occupied trigonal-bipyramidal sites, Mater. Res. Bull. 3 (1968) 409–415.

[13] L.C. Upadhyayula, J.J. Loferski, A. Wold, W. Giriat, R. Kershaw, Semiconducting properties of single crystals of n- and p-type tungsten diselenide ($WSe_2$), J. Appl. Phys. 39 (1968) 4736–4740.

[14] W.H. Strehlow, E.L. Cook, Compilation of energy band gaps in elemental and binary compound semiconductors and insulators, J. Phys. Chem. Ref. Data 2 (1973) 163–200.

[15] A. Jäger-Waldau, E. Bucher, $WSe_2$ thin films prepared by soft selenization, Thin Solid Films 200 (1991) 157–164.

[16] A.R. Beal, W.Y. Liang, Excitons in 2H-$WSe_2$ and 3R-$WS_2$, J. Phys. C 9 (1976) 2459–2466.

[17] C. Chiritescu, D.G. Cahill, N. Nguyen, D. Johnson, A. Bodapati, P. Keblinski, P. Zschack, Ultralow thermal conductivity in disordered, layered $WSe_2$ crystals, Science 315 (2007) 351–353.

[18] A. Jain, S.P. Ong, G. Hautier, W. Chen, W.D. Richards, S. Dacek, S. Cholia, D. Gunter, D. Skinner, G. Ceder, K.A. Persson, Commentary: the materials project: a materials genome approach to accelerating materials innovation, Apl. Mater. 1 (2013), 011002.

[19] H. Wang, D. Kong, P. Johanes, J.J. Cha, G. Zheng, K. Yan, N. Liu, Y. Cui, $MoSe_2$ and $WSe_2$ nanofilms with vertically aligned molecular layers on curved and rough surfaces, Nano Lett. 13 (2013) 3426–3433.

[20] M.A. Lukowski, A.S. Daniel, C.R. English, F. Meng, A. Forticaux, R.J. Hamers, S. Jin, Highly active hydrogen evolution catalysis from metallic $WS_2$ nanosheets, Energy Environ. Sci. 7 (2014) 2608–2613.

[21] S.T. Finn, J.E. Macdonald, Contact and support considerations in the hydrogen evolution reaction activity of petaled $MoS_2$ electrodes, ACS Appl. Mater. Interfaces 8 (2016) 25185–25192.

[22] W. Zhao, R.M. Ribeiro, M. Toh, A. Carvalho, C. Kloc, A.H.C. Neto, G. Eda, Origin of indirect optical transitions in few-layer $MoS_2$, $WS_2$, and $WSe_2$, Physics 13 (2013) 5627–5634.

[23] S. Dominguez-Meister, A. Justo, J. Sanchez-Lopez, Synthesis and tribological properties of $WSe_x$ films prepared by magnetron sputtering, Science 142 (2013) 186–194.

[24] H. Tributsch, Layer-type transition metal dichalcogenides—a new class of electrodes for electrochemical solar cells, Phys. Chem. 8 (1977) 361–369.

[25] W. Jaegermann, H. Tributsch, Interfacial properties of semiconducting transition metal chalcogenides, Surf. Sci. 29 (1988) 1–167.

[26] A. Klein, Y. Tomm, R. Schlaf, C. Pettenkofer, W. Jaegermann, M. Lux-Steiner, E. Bucher, Photovoltaic properties of $WSe_2$ single crystals studied by photoelectron spectroscopy, Sol. Energy Mater. Sol. Cells 51 (1998) 181–191.

[27] J. Pouzet, J. Bernede, A. Khellil, H. Essaidi, S. Benhida, Preparation and characterization of tungsten diselenide thin films, Thin Solid Films 208 (1992) 252–259.

[28] G. Salitra, G. Hodes, E. Klein, R. Tenne, Highly oriented $WSe_2$ thin films prepared by selenization of evaporated $WO_3$, Thin Solid Films 245 (1994) 180–185.

[29] P. Patel, J. Rathod, H.S. Patel, K. Patel, V. Pathak, Structural and optical characterization of tungsten diselenide crystals grown by DVT technique, Adv. Mater. Res. 665 (2013) 53–57.

[30] P. Hankare, A. Manikshete, D. Sathe, P. Chate, K. Rathod, Novel chemical synthetic route and characterization of tungsten diselenide thin films, Mater. Chem. Phys. 113 (2009) 183–186.

[31] J.J. Devadasan, C. Sanjeeviraja, M. Jayachandran, Electrosynthesis and characterization of n-$WSe_2$ thin films, Mater. Chem. Phys. 77 (2003) 397–401.

[32] S. Grigoriev, V. Fominski, A. Gnedovets, R. Romanov, Experimental and numerical study of the chemical composition of $WSe_x$ thin films obtained by pulsed laser deposition in vacuum and in a buffer gas atmosphere, Appl. Surf. Sci. 258 (2012) 7000–7007.

[33] P. Browning, S. Eichfeld, K. Zhang, L. Hossain, Y.-C. Lin, K. Wang, N. Lu, A.R. Waite, A.A. Voevodin, M. Kim, J.A. Robinson, Largearea synthesis of $WSe_2$ from $WO_3$ by selenium–oxygen ion exchange, 2D Mater. 2 (2015), 014003.

[34] N.D. Boscher, C.J. Carmalt, I.P. Parkin, Atmospheric pressure chemical vapor deposition of $WSe_2$ thin films on glass—highly hydrophobic sticky surfaces, J. Mater. Chem. 16 (2006) 122–127.

[35] H. Li, D. Gao, S. Xie, J. Zou, Effect of magnetron sputtering parameters and stress state of W film precursors on $WSe_2$ layer texture by rapid selenization, Sci. Rep. 6 (2016), 36451.

[36] H. Li, D. Gao, K. Li, M. Pang, S. Xie, R. Liu, J. Zou, Texture control and growth mechanism of $WSe^2$ film prepared by rapid selenization of W film, Appl. Surf. Sci. 394 (2017) 142–148.

[37] R. Cheng, D. Li, H. Zhou, C. Wang, A. Yin, S. Jiang, Y. Liu, Y. Chen, Y. Huang, X. Duan, Electroluminescence and photocurrent generation from atomically sharp $WSe_2$/$MoS_2$ heterojunction p–n diodes, Nano Lett. 14 (2014) 5590–5597.

[38] H. Fang, S. Chuang, T.C. Chang, K. Takei, T. Takahashi, A. Javey, High-performance single layered $WSe_2$ p-FETs with chemically doped contacts, Nano Lett. 12 (2012) 3788–3792.

[39] A.-J. Cho, K.C. Park, J.-Y. Kwon, A high-performance complementary inverter based on transition metal dichalcogenide field-effect transistors, Nanoscale Res. Lett. 10 (2015) 115.

[40] L. Yu, A. Zubair, E.J.G. Santos, X. Zhang, Y. Lin, Y. Zhang, T. Palacios, High-performance $WSe_2$ complementary metal oxide semiconductor technology and integrated circuits, Nano Lett. 15 (2015) 4928–4934.

[41] M.M. Furchi, A. Pospischil, F. Libisch, J. Burgdörfer, T. Mueller, Photovoltaic effect in an electrically tunable van der Waals heterojunction, Nano Lett. 14 (2014) 4785–4791.

[42] M.-L. Tsai, M.-Y. Li, J.R.D. Retamal, K.-T. Lam, Y.-C. Lin, K. Suenaga, L.-J. Chen, G. Liang, L.-J. Li, J.-H. He, Single atomically sharp lateral monolayer p-n heterojunction solar cells with extraordinarily high-power conversion efficiency, Adv. Mater. 29 (2017), 1701168.

[43] H. Kyureghian, M. Hilfiker, E. Ediger, V. Medic, N. Ianno, Numerical modeling of WSe2 solar cells, in: IEEE 44th Photovoltaic Specialist Conference (PVSC), 2017, pp. 2364–2367.

[44] M. Burgelman, P. Nollet, S. Degrave, Modelling polycrystalline semiconductor solar cells, Thin Solid Films 361–362 (2000) 527–532.

[45] S. Vallisree, R. Thangavel, l.T. Lenka, Modelling, simulation, optimization of Si/ ZnO and Si/ZnMgO heterojunction solar cells, Mater. Res. Express 6 (2018), 025910.

[46] A. Kuddus, M.F. Rahman, S. Ahmmed, J. Hossain, A.B.M. Ismail, Role of facile synthesized $V_2O_5$ as hole transport layer for CdS/CdTe heterojunction solar cell: validation of simulation using experimental data, Superlattice. Microst. 132 (2019), 106168.

[47] Y. Gan, X. Bi, Y. Liu, B. Qin, Q. Li, Q. Jiang, P. Mo, Numerical investigation energy conversion performance of tin-based perovskite solar cells using cell capacitance simulator, Energies 13 (2020) 5907.

[48] M.F.M. Noh, C.H. Teh, R. Daik, E.L. Lim, C.C. Yap, M.A. Ibrahim, N.A. Ludin, A.R. bin Mohd Yusoff, J. Jang, M.A.M. Teridi, The architecture of the electron transport layer for a perovskite solar cell, J. Mater. Chem. C 6 (2018) 682–712.

[49] J.P.C. Baena, L. Steier, W. Tress, M. Saliba, S. Neutzner, T. Matsui, F. Giordano, T.J. Jacobsson, A.R.S. Kandada, S.M. Zakeeruddin, et al., Highly efficient planar perovskite solar cells through band alignment engineering, Energy Environ. Sci. 8 (2015) 2928–2934.

[50] Q. Ma, H. Kyureghian, J.D. Banninga, N.J. Ianno, Thin film $WSe_2$ for use as a photovoltaic absorber material, MRS Online Proc. Libr. 1670 (2014) 77–82.

[51] S. Masudy-Panah, K. Radhakrishnan, A. Kumar, T.I. Wong, R. Yi, G.K. Dalapati, Optical bandgap widening and phase transformation of nitrogen doped cupric oxide, J. Appl. Phys. 118 (2015), 225301.

[52] H. Li, C. Pu, C. Ma, S. Li, W. Dong, S. Bao, Q. Zhang, Growth behavior and optical properties of N-doped $Cu_2O$ films, Thin Solid Films 520 (2011) 212–216.

[53] Ø. Nordseth, R. Kumar, K. Bergum, I. Chilibon, S.E. Foss, E. Monakhov, Nitrogen-doped $Cu_2O$ thin films for photovoltaic applications, Materials 12 (2019) 3038.

[54] Y. Yi, C. Wu, H. Liu, J. Zeng, H. He, J. Wang, A study of lateral Schottky contacts in $WSe_2$ and $MoS_2$ field effect transistors using scanning photocurrent microscopy, Nanoscale 7 (2015) 15711–15718.

[55] D.S. Ginley, J.D. Perkins, Transparent conductors, in: Handbook of Transparent Conductors, Springer, 2011, pp. 1–25.

[56] R. Chaurasiya, G.K. Gupta, A. Dixit, Ultrathin janus WSSe buffer layer for W(S/Se)$_2$ absorber based solar cells: a hybrid, DFT and macroscopic, simulation studies, Sol. Energy Mat. And Slo. Cells 201 (2019), 110076.

[57] H. Tang, K. Prasad, R. Sanjines, P. Schmid, F. Levy, Electricalandoptical properties of $TiO_2$ anatase thin films, J. Appl. Phys. 75 (1994) 2042–2047.

[58] S.V. Farahani, T. Veal, J. Mudd, D. Scanlon, G. Watson, O. Bierwagen, M. White, J. Speck, C. McConville, Valence-band density of states and surface electron accumulation in epitaxial SnO$_2$ films, Phys. Rev. B 90 (2014), 155413.

[59] H.B. Michaelson, The work function of the elements and its periodicity, J. Appl. Phys. 48 (1977) 4729–4733.

[60] M. Vogt, M.C. Lux-Steiner, P. Dolatzoglou, E. Bucher, Comparison between the photovoltaic performance of WSe2 heterojunctions perpared by ITO or ZnO magnetron sputtering, in: Proceed. Of the 8th E.C. Photovolatic Energy Conference, Florence, Italy, 1988, p. 1112.

[61] A. Jakubowicz, D. Mahalu, M. Wolf, A. Wold, R. Tenne, WSe$_2$: optical and electrical properties as related to surface passivation of recombination centers, Phys. Rev. B 40 (1989) 2992–3000.

[62] S. Masudy-Panah, K. Radhakrishnan, A. Kumar, T.I. Wong, R. Yi, G.K. Dalapati, Optical bandgap widening and phase transformation of nitrogen doped cupric oxide, J. Appl. Phys. 118 (2015), 225301.

[63] J. Gong, X. Wang, X. Fan, R. Dai, Z. Wang, Z. Zhang, Z. Ding, Temperature dependent optical properties of SnO$_2$ film study by ellipsometry, Opt. Mater. Express 9 (2019) 3691.

[64] Y. Bouachiba, A. Bouabellou, F. Hanini, F. Kermiche, A. Taabouche, K. Boukheddaden, Structural and optical properties of TiO$_2$ thin films grown by sol-gel dip coating process, Mater. Sci-Pol. 32 (2014) 1–6.

[65] A.E. Kissani, H.A. Dads, S. Oucharrou, F. Welatta, H. Elaakib, L. Nkhaili, A. Narjis, A. Khalfi, K.E. Assail, A. Outzourhit, A facile route for synthesis of cadmium sulfide thin films, Thin Solid Films 664 (2018) 66–69.

[66] Munirah, Z.R. Khan, A. Aziz, M.S. Khan, M. Khandaker, Influence of zinc concentration on band gap and sub-band gap absorption on ZnO nanocrystalline thin films sol-gel grown, Mater. Sci-Pol. 35 (2017) 246–253.

[67] J. Kessler, M. Ruckh, D. Hariskos, U. Ruhle, R. Menner, H. Schock, Interface engineering between CuInSe$_2$ and ZnO, in: Conference Record of the Twenty Third IEEE Photovoltaic Specialists Conference - 1993 (Cat. No.93CH3283-9), 1993, pp. 447–452.

[68] W.-Y. Rho, H. Jeon, H.-S. Kim, W.-J. Chung, J.S. Suh, B.-H. Jun, Recent progress in dye-sensitized solar cells for improving efficiency: TiO$_2$ nanotube arrays in active layer, J. Nanomater. 2015 (2015).

[69] S.K. Pathak, A. Abate, P. Ruckdeschel, B. Roose, K.C. Gödel, Y. Vaynzof, A. Santhala, S.-I. Watanabe, D.J. Hollman, N. Noel, et al., Performance and stability enhancement of dye-sensitized and perovskite solar cells by al doping of TiO$_2$, Adv. Funct. Mater. 24 (2014) 6046–6055.

[70] T. Bak, M.K. Nowotny, L.R. Sheppard, J. Nowotny, Mobility of electronic charge carriers in titanium dioxide, J. Phys. Chem. C 112 (2008) 12981–12987.

[71] R. Li, Y. Zhou, M. Sun, Z. Gong, Y. Guo, F. Wu, W. Li, W. Ding, Influence of charge carriers concentration and mobility on the gas sensing behavior of tin dioxide thin films, Coatings 9 (2019) 591.

[72] H. Mun, H. Yang, J. Park, C. Ju, K. Char, High electron mobility in epitaxial SnO$_{2-x}$ in semiconducting regime, Apl. Mater. 3 (2015), 076107.

[73] J. Heo, A.S. Hock, R.G. Gordon, Low temperature atomic layer deposition of tin oxide, Chem. Mater. 22 (2010) 4964–4973.

[74] Y.H. Khattak, F. Baig, H. Toura, S. Beg, B.M. Soucase, CZTSe kesterite as an alternative hole transport layer for MASnI$_3$ perovskite solar cells, J. Electron. Mater. 48 (2019) 5723–5733.

[75] M. Turcu, U. Rau, Fermi level pinning at CdS/Cu(In,Ga)(Se,S)$_2$ interfaces: effect of chalcopyrite alloy composition, J. Phys. Chem. Solid. 64 (2003) 1591–1595.

[76] U. Rau, H. Schock, Electronic properties of Cu(In,Ga)Se$_2$ heterojunction solar cells-recent achievements, current understanding, and future challenges, Appl. Phys. A 69 (1999) 131–147.

[77] T. Minemoto, T. Matsui, H. Takakura, Y. Hamakawa, T. Negami, Y. Hashimoto, T. Uenoyama, M. Kitagawa, Theoretical analysis of the effect of conduction band offset of window/CIS layers on performance of CIS solar cells using device simulation, Sol. Energy Mater. Sol. Cell. 67 (2001) 83–88.

[78] A. Kumar, Efficiency enhancement of CZTS solar cells using structural engineering, Superlattice, Micro 153 (2021), 106872.

[79] X.-B. Xu, X.-Y. Wang, W.-P. Gu, S. Quan, Z. Zhang, Study on influences of CdZnS buffer layer on CdTe solar cells, Superlattice, Micro 109 (2017) 463–469.

[80] D. Liu, M.K. Gangishetty, T.L. Kelly, Effect of CH$_3$NH$_3$PbI$_3$ thickness on device efficiency in planar heterojunction perovskite solar cells, J. Mater. Chem. 2 (2014) 19873–19881.

[81] L.M. Pazos-Outon, T.P. Xiao, E. Yablonovitch, Fundamental efficiency limit of lead iodide perovskite solar cells, J. Phys. Chem. Lett. 9 (2018) 1703–1711.

[82] R. Jeyakumar, A. Bag, R. Nekovei, R. Radhakrishnan, Interface studies by simulation on methylammonium lead iodide based planar perovskite solar cells for high efficiency, Sol. Energy 190 (2019) 104–111.

[83] W.H. Nguyen, C.D. Bailie, E.L. Unger, M.D. McGehee, Enhancing the hole-conductivity of spiro-ometad without oxygen or lithium salts by using spiro (TFSI)$_2$ in perovskite and dye-sensitized solar cells, J. Am. Chem. Soc. 136 (2014) 10996–11001.

[84] S. Nann, K. Emery, Spectral effects on PV-device rating, Sol. Energy Mater. Sol. Cell. 27 (1992) 189–216.

[85] S. Chander, A. Purohit, A. Sharma, S. Nehra, M. Dhaka, etal, Astudy on photovoltaic parameters of mono-crystalline silicon solar cell with cell temperature, Energy Rep. 1 (2015) 104–109.

[86] K. Emery, C. Osterwald, Measurement of photovoltaic device current as a function of voltage, temperature, intensity and spectrum, Sol. Cell. 21 (1987) 313–327.

[87] Y. Tsuno, Y. Hishikawa, K. Kurokawa, Temperature and irradiance dependence of the IV curves of various kinds of solar cells, Techn. Digest PVSEC 15 (2005) 422–423.

[88] U.A. Yusufoglu, T.M. Pletzer, L.J. Koduvelikulathu, C. Comparotto, R. Kopecek, H. Kurz, Analysis of the annual performance of bifacial modules and optimization methods, IEEE J. Photovoltaics 5 (2014) 320–328.

[89] X. Sun, M.R. Khan, C. Deline, M.A. Alam, Optimization and performance of bifacial solar modules: a global perspective, Appl. Energy 212 (2018) 1601–1610.

[90] M. Fischer, ITRPV 9th edition 2018 report release and key findings, in: PV CellTech Conference, vol. 14, 2018.

[91] Y.S. Lee, J. Heo, M.T. Winkler, S.C. Siah, S.B. Kim, R.G. Gordon, T. Buonassisi, Nitrogen-doped cuprous oxide as a p-type hole transporting layer in thin-film solar cells, J. Mater. Chem. 1 (2013) 15416–15422.

[92] M.-J. Dai, S.-S. Lin, Q. Shi, F. Liu, W.-X. Wang, S.-C. Chen, T.-Y. Kuo, H. Sun, Transparent conductive p-type cuprous oxide films in vis-nir region prepared by ion-beam assisted dc reactive sputtering, Coatings 10 (2020) 473.

[93] G.G. U., et al., Bifacial concentrator Ag-free crystalline n-type Si solar cell, Prog. Photovoltaics Res. Appl. 23 (2015) 600–610.

[94] A.M. Baldridge, S. Hook, C. Grove, G. Rivera, The ASTER spectral library version 2.0, Rem. Sens. Environ. 113 (2009) 711–715.

[95] A.B. Phillips, K.K. Subedi, G.K. Liyanage, F.K. Alfadhili, R.J. Ellingson, M.J. Heben, Understanding and advancing bifacial thin film solar cells, ACS Appl. Energy Mater. 3 (2020) 6072–6078.